Volume 27
Number 20
28 May 2025
Pages 10429–10898

PCCP

Physical Chemistry Chemical Physics

rsc.li/pccp

25 YEARS ANNIVERSARY

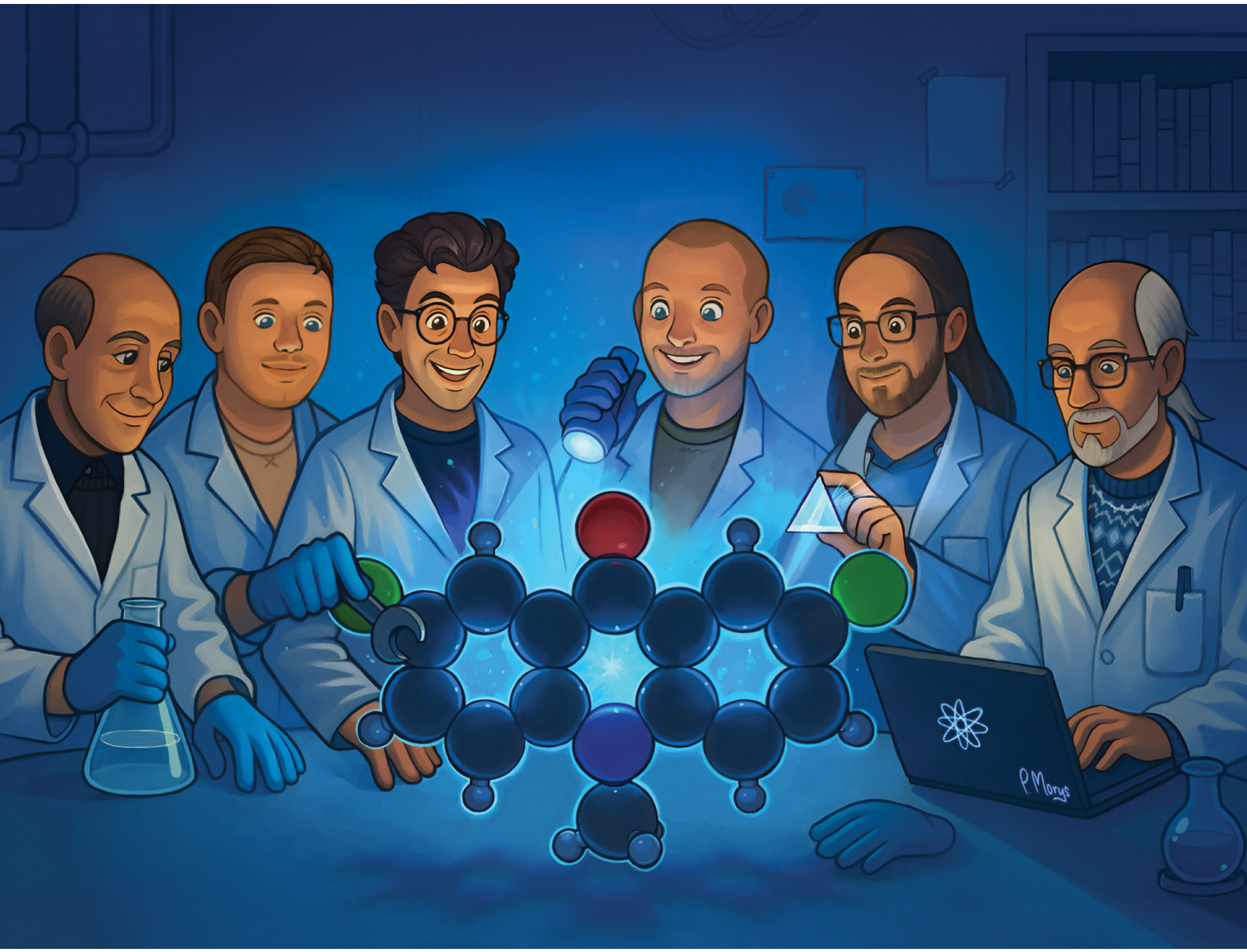

ISSN 1463-9076

ROYAL SOCIETY OF CHEMISTRY

PAPER
Peter Gilch *et al.*
Substituted acridones: simple deep blue HIGHrISC emitters in an aprotic environment

PCCP Owner Societies

PCCP

PAPER

View Article Online
View Journal | View Issue

Cite this: *Phys. Chem. Chem. Phys.*, 2025, **27**, 10444

Substituted acridones: simple deep blue HIGHrISC emitters in an aprotic environment†

Matthias Jantz, ‡[a] David Klaverkamp, ‡[a] Lennart Bunnemann, ‡[b] Martin Kleinschmidt, [c] Constantin Czekelius [b] and Peter Gilch *[a]

Received 19th December 2024,
Accepted 5th March 2025

DOI: 10.1039/d4cp04781h

rsc.li/pccp

N-Methylacridones (NMAs) substituted at positions 2 and 7 with +M groups (fluorine and methoxy) were synthesized and characterized by steady-state and time-resolved spectroscopy. Solutions of the NMA derivatives in an aprotic solvent (tetrahydrofuran) emit in the deep blue region of the visible spectrum with radiative rate constants larger than 5.4×10^7 s^{-1} and fluorescence quantum yields up to 0.84. Sensitization experiments employing 1,4-dichlorobenzene give evidence for HIGHrISC behavior of the NMAs, that is, reverse intersystem crossing (rISC) from a higher triplet state $T_{n\geq 2}$ occurs. The spectroscopic results, which are corroborated by quantum chemical calculations, render these derivatives very promising for applications in organic light emitting diodes (OLEDs).

Introduction

With the HIGHrISC[1,2] or hot exciton[3,4] approach, triplet excitons can be converted into light. This is of particular interest in organic light-emitting diodes (OLEDs) in which $\frac{3}{4}$ of the excitons formed by electron–hole recombination adopt triplet spin multiplicity.[5] In HIGHrISC emitters, reverse intersystem crossing (rISC) from a higher triplet state $T_{n\geq 2}$ to the emissive singlet state S_1 occurs (*cf.* Fig. 1). For HIGHrISC to be efficient, its respective rate constant k_{rISC} ought to be larger than the one for internal conversion (IC) k_{IC} between the T_n and the lowest triplet state T_1. Furthermore, the T_n state should be slightly (a few times the thermal energy k_BT) higher in energy than the S_1 state.[1] This ensures that after equilibration of the two states, most of the population resides in the emissive S_1 state. El-Sayed-allowed transitions as occurring in carbonyl compounds promise large ISC and thereby also rISC rate constants.[6,7] For an emission in the visible range, the carbonyl group ought to be part of a polyaromatic scaffold of the size of anthracene or lager.[7] For the closely related aromatic carbonyl compounds xanthones,[8] thioxanthones,[1] and acridones[2] HIGHrISC activity was observed by us. All these compounds emit in the blue region of the visible spectrum. Acridones are particularly promising in this respect as some derivatives dissolved in suitable solvents feature fluorescence quantum yields ϕ_{fl} close to one.[9] The focus of this study will be on derivatives of *N*-methylacridone (NMA). Contrary to the parent compound acridone, NMA lacks a an NH group which can act as a hydrogen bond donor.

When inspecting the excited state energies of NMA in the gas phase,[10] high fluorescence quantum yields ϕ_{fl} in solution seem surprising. In NMA, the emissive singlet state is a $^1\pi\pi^*$ one. Three essentially dark states ($^1n\pi^*$, $^3n\pi^*$, and $^3\pi\pi^*$) are lower in energy. Thus, the $^1\pi\pi^*$ state may depopulate *via* a $^1\pi\pi^* \rightarrow {}^1n\pi^*$ IC process. Femtosecond spectroscopy of the closely related thioxanthone has shown that such an IC process may occur in a few 100 fs.[11] Also, the El-Sayed-allowed $^1\pi\pi^* \rightarrow {}^3n\pi^*$ transition can contribute to a fast $^1\pi\pi^*$ depopulation.[12,13] For NMA to exhibit high fluorescence quantum yields ϕ_{fl} and HIGHrISC activity the $n\pi^*$ states (singlet and triplet) need to be lifted in energy above the $^1\pi\pi^*$ one. As the energetic separations (in the gas phase) amount to only 1200 cm^{-1} (0.15 eV, $^1\pi\pi^*$–$^1n\pi^*$) and 2300 cm^{-1} (0.28 eV, $^1\pi\pi^*$–$^3n\pi^*$),[10] respectively, rather small modifications of the molecule or its surroundings can suffice to achieve this goal. Indeed, polar protic solvents can invert the energetic ordering of $^1\pi\pi^*$ and $^{1,3}n\pi^*$ states.[14] However, theoretical[14] and experimental studies[15] disagree with respect to the polarity which is needed to invert the ordering of states. The $^1\pi\pi^*$ excitation in acridones goes along with an increase of the dipole moment[14,16] and thus experiences a red-shift with increasing solvent polarity. $^{1,3}n\pi^*$-Excitations commonly,[17,18] particularly in acridones,[9] experience a blue shift in polar and – most pronounced – protic solvents. These opposite shifts cause both $n\pi^*$ states of NMA in protic solvents to lie above the $^1\pi\pi^*$ one in energy.[14] The most visible consequence of this is the strongly increased fluorescence quantum yield ϕ_{fl} of NMA in protic solvents ($\phi_{fl} \approx 0.7$ in methanol)[19] as compared to nonpolar ones ($\phi_{fl} \approx$

[a] *Institut für Physikalische Chemie, Heinrich-Heine-Universität Düsseldorf, Universitätsstr. 1, 40225 Düsseldorf, Germany. E-mail: gilch@hhu.de*
[b] *Institut für Organische Chemie und Makromolekulare Chemie, Heinrich-Heine-Universität Düsseldorf, Universitätsstr. 1, 40225 Düsseldorf, Germany*
[c] *Institut für Theoretische Chemie und Computerchemie, Heinrich-Heine-Universität Düsseldorf, Universitätsstr. 1, 40225 Düsseldorf, Germany*

† Electronic supplementary information (ESI) available. See DOI: https://doi.org/10.1039/d4cp04781h

‡ These authors contributed equally to this work.

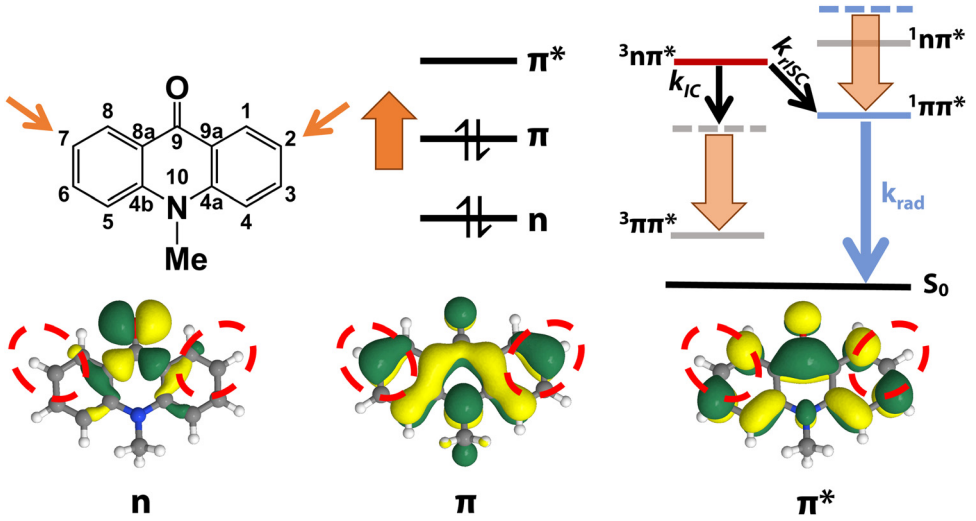

Fig. 1 Illustration of the impact of +I/+M substituents at positions 2 and 7 on the NMA excitation energies. The depiction of the molecular orbitals on the bottom (adapted from ref. 10) indicates that only the π-orbital features electron density at positions 2 and 7 (encircled in red).

0.02 in cyclohexane).[9] With respect to OLEDs, relying on protic solvents is problematic, however. In OLEDs chromophores are embedded in rather nonpolar and aprotic matrices.[20–22]

To achieve this inversion in an aprotic environment the ^{1}ππ* energy can be lowered by placing substituents with a positive inductive effect (+I) and/or with a positive mesomeric effect (+M) at suitable positions (Fig. 1).[23] The positions can be identified by inspection of the frontier orbitals (*cf.* Fig. 1). At the positions 2 and 7, the HOMO (π-orbital) features anti-nodes and the LUMO (π*-orbital) nodes. Thus, in a simplified picture, +M substituents placed here are expected to rise the energy of the π-orbital and leave the one of the π*-orbital untouched. This ought to result in the lowering of the ^{1}ππ* energy. Indeed, difluorination (+M effect)[24] of NMA at positions 2 and 7 shifts the ^{1}ππ* 0–0 energy by −1130 cm^{-1} (−0.14 eV, value refers to the compounds dissolved in methanol).[19] A quantum chemical investigation on substituent effects on the excitation energy of anthracene – a chromophore of similar size – predicted shifts of the same magnitude.[25] The measured red-shift of −1130 cm^{-1} (−0.14 eV) has the same magnitude as the ^{1}ππ*–^{1,3}nπ* separations mentioned above. Thus, an inversion of the state ordering and a shift into the deep blue region[26] of the visible spectrum might be achievable by substitution. By introducing other groups with a +M effect, like methoxy,[27] a stronger inversion of the ordering and a greater energetic separation of the states might be attained. Moreover, the emission should be shifted further into the deep blue. Therefore, in addition to the NMA-dF, new derivatives (for structures see Fig. 2) were investigated: one, where one fluorine is exchanged for a methoxy substituent (NMA-OMeF) and one, where both fluorine atoms are exchanged for methoxy substituents (NMA-dOMe). As already mentioned, the inversion of the states should be caused by substituents and not by the formation of hydrogen bonds between the NMA derivatives and the solvent. For this reason, tetrahydrofuran (THF) was chosen as the solvent due to its aprotic nature. Additionally, THF offers a deep UV cutoff[28] and its polarity is similar to the one present in an OLED,[29] making it an appropriate choice for the study.

In this study, the photophysical properties of NMA, NMA-dF, NMA-OMeF and NMA-dOMe in THF were investigated. For this purpose, stationary absorption and emission spectra were recorded. In addition, time-resolved spectroscopy in the femtosecond and nanosecond regime was performed and a comparison between direct and sensitized excitation was made. For sensitized excitation, 1,4-dichlorobenzene (DCB) was employed as a triplet sensitizer. Triplet-excited DCB serves as a substitute for triplet-correlated electron–hole pairs in an OLED. It is crucial to note, that DCB is not supposed to be utilized in an actual device. Rather, the upper triplet state is directly populated by electron–hole recombination. The results will show that the substituted acridones can convert both singlet and triplet excitons into light even in an aprotic environment. The experimental results are complemented by quantum chemical calculations.

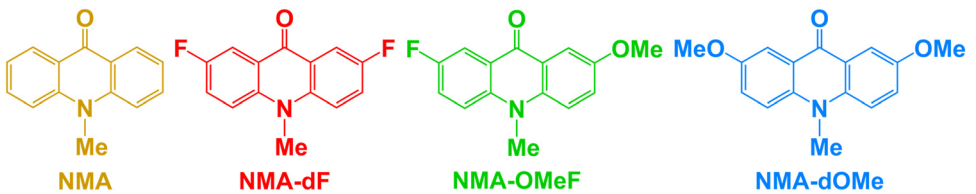

Fig. 2 Structural formulas of the various *N*-methylated acridones (NMA) used in this study.

Materials and methods

Steady state spectroscopy

The UV/Vis absorption spectra were measured using a two-beam Lambda 1050+ spectrometer from PerkinElmer GmbH, utilizing standard 1-cm path-length fused silica cells. Fluorescence was recorded in right-angle detection mode with a FluoroMax-4 from Horiba Scientific. To prevent inner filter effects, the absorption at the excitation wavelength was adjusted to $\sim$0.05 for a 1 cm path length. Coumarin 102 in air-saturated ethanol (ϕ_{fl} = 0.764)[30] served as the reference for determining the fluorescence quantum yields of the NMAs. All emission spectra were corrected for the spectral sensitivity of the instrument. To determine the 0–0 energies and Stokes shifts, the fluorescence spectra were multiplied by λ^2 to convert them from a constant wavelength bandpass to a constant wavenumber bandpass.[31] Furthermore, the absorption spectra were multiplied by $\tilde{\nu}^{-1}$ and the fluorescence spectra by $\tilde{\nu}^{-3}$ to arrive at the transition dipole representation.[32] The 0–0 energies were obtained by the intersection between the absorption and fluorescence spectra in this representation, which were normalized to their respective maxima. Strickler–Berg analysis were conducted according to ref. 33 and 34, wherein only the absorption bands lowest in energy were included. The CIE coordinates were determined using the respective emission spectra and the ARL Spectral Fitting software.[35]

Time-resolved absorption spectroscopy

The femtosecond transient absorption (fsTA) setup has been described elsewhere.[36] Thus, here only a brief summary is given which focuses on the settings relevant for this study. A 1 kHz Ti:Sa laser amplifier system (Coherent Libra) served as the pulse source, emitting at a wavelength of 800 nm with a pulse duration of 120 fs (full width at half maximum (FWHM)). To produce 400 nm pump pulses, the 800 nm laser output underwent frequency doubling in a β-barium borate crystal. The energy of the pump pulse at the sample was adjusted to approximately 1 μJ, and the beam had a focal diameter of 160 μm on the sample. The absorption change was probed using a white light continuum generated in CaF_2, with a diameter of 100 μm at the sample. The relative polarization of the pump and probe beams was set to the magic angle to avoid contributions from rotational diffusion. The time resolution of the measurements was approximately 150 fs (FWHM of the instrument response function (IRF)). Transient spectra were recorded at 139-time delay settings, spanning from −1 to 1 ps on a linear time scale, and from 1 ps to 3.4 ns on a logarithmic one. For each delay setting, 2000 spectra were recorded, and the data were averaged over four successive delay scans. To eliminate solvent signal contributions and correct for time-zero femtosecond artifacts, a solvent measurement was conducted. Its signal was subtracted from the one of the solution after proper scaling.[37] The sample solutions were pumped through a silica flow cell (Hellma Analytics) with a path length of 0.5 mm. The absorption of the sample at the excitation wavelength was adjusted to $\sim$0.7 for a path length of 0.5 mm. Time constants and decay-associated difference spectra (DADS) were obtained using a global fitting procedure with a multi-exponential trial function convoluted with the IRF (see eqn (1)),[38]

$$\Delta A(\lambda, t) = \mathrm{IRF} \otimes \sum_{i=1}^{n} \Delta A_i(\lambda) \cdot \mathrm{e}^{-\frac{t}{\tau_i}}. \quad (1)$$

The fit yields a decay associated difference spectrum (DADS) $\Delta A_i(\lambda)$ for each time constant τ_i.

Nanosecond transient absorption (nsTA) data were obtained with a LP980 spectrometer from Edinburgh Instruments. For the excitation, the output of a Nd:YAG laser (Spitlight 600, Innolas) was frequency-quadrupled to arrive at 266 nm. The laser provides pulses with a duration of $\sim$7 ns at a repetition rate of 10 Hz. The average pulse energy amounted to $\sim$3 mJ. A pulsed xenon flashlamp (Osram XBO 150 W/CROFR) was used for probing. After passing the sample at a right-angle geometry, the light was dispersed in a grating monochromator and detected by a photomultiplier (Hamamatsu PMT-900). The time resolution was approximately 7 ns (FWHM of the IRF). For NMA-OMeF solutions, the pathlengths of the flow cell were 2 mm in pump and 10 mm in probe direction. For DCB solutions, the pathlengths of the flow cell were 5 mm in pump and 10 mm in probe direction. To obtain the triplet lifetime of NMA-OMeF for each of the four different concentrations twelve time traces were recorded at a probe wavelength of 585 nm. For each time trace 64 shots were averaged. To obtain the self-quenching constant of DCB, the rate constants of the triplet decay were determined for four different concentrations. For each concentration, ten time traces were recorded at 340 nm. For each time trace 80 shots were averaged.

Time-resolved emission spectroscopy

Time-correlated single photon counting (TCSPC) was conducted utilizing a fluorescence lifetime and steady-state spectrometer (FT300 with hybrid PMT detector, Pico Quant, Germany). The excitation process was accomplished using a supercontinuum laser excitation source (EXW-12 with a spectral extension unit EXTEND-UV, NKT Photonics, Denmark) operating at a repetition rate of 4.88 MHz. The output of the supercontinuum laser was frequency-doubled and excitation wavelengths were selected by a monochromator. The wavelengths were chosen to match the different absorption maxima: 375 nm, 416 nm, 424 nm, and 429 nm for NMA, NMA-dF, NMA-OMeF, and NMA-dOMe, respectively. Input and output slit widths of the monochromator were set to 3000 μm, resulting in a detection bandpass of 16.2 nm. The detection wavelengths were set to coincide with the fluorescence maxima for NMA (405 nm), NMA-OMeF (446 nm) and NMA-dOMe (457 nm). The detection wavelength for NMA-dF was set to 450 nm. The emission maximum was not chosen here, as it coincides with the Raman band of the solvent, generating an additional signal. The IRF was determined using a Ludox HS-30 colloidal silica water suspension (Aldrich), featuring a ''zero'' lifetime. The FWHM of the IRF was approximately 100 ps, and its influence was factored into the fitting process through convolution. Quartz Macro Cell type 111-QS cuvettes (Hellma) were employed for all sample measurements, featuring a light path of 1 cm and a sample volume of 3 mL. Fitting procedures were

executed using the ChiSurf software.[39] A single exponential including an offset which accounts for detector dark counts and after-pulsing served as a trial function.

Time-resolved fluorescence data from the nano- to microsecond regime were acquired with a home-built setup. For the excitation, the pulsed Nd:YAG laser (Spitlight 600, Innolas) mentioned above tuned to 266 nm was used, providing pulses of ~7 ns FWHM at a repetition rate of 10 Hz. The energy of the laser light was ~125 μJ per pulse. The excitation beam was focused onto the sample with a cylindrical lens generating a line focus 0.5 mm wide and 2.5 mm long. The emitted fluorescence light was collected under an angle of 54°, then dispersed by a spectrograph (SpectraPro 308, Acton Research) with a grating blazed at 410 nm (121.6 l mm^{-1}) and detected by a gated iCCD camera (PI-MAX, Princeton Instruments). The delay between excitation and detection was controlled electronically (PTG, Princeton Instruments) and enabled delay times from the nanosecond to the millisecond regime. To increase the signal at longer delay times the gain voltage of the microchannel plate was raised. Besides that, the integration time of the detector as well as the number of accumulations were increased for longer delay times. The signals from the CCD chip's pixel rows, where fluorescence light was detected, were summed up (200 rows), and the resulting spectra were spectrally integrated over the emission band of interest. The data were corrected for the baseline by subtracting the integrated signal from rows of the CCD chip where no fluorescence signal was detected. The baseline-corrected data were divided by the number of accumulations and by the integration time applied. To account for the varying gain voltage, a calibration curve was generated using the same instrumental parameters expect for different amplification settings U_{MCP}, ranging from 0 to 255. The spectrally integrated fluorescence signal $S_{int}(U_{MCP})$ in dependence of U_{MCP} was fitted to an exponential function according to eqn (2),

$$S_{int}(U_{MCP}) = \alpha \cdot e^{\beta \cdot U_{MCP}}. \quad (2)$$

For the various measurements, α and β are listed in Table S1 (ESI†). To correct for this dependency, each data point was divided by the right-hand-side of eqn (2). To cross-check the procedure, blocks for delay time ranges and certain settings U_{MCP} overlapped slightly. For the overlapping part, signals of blocks were compared and if necessary slightly scaled to match each other. For the characterization of the IRF, a solution of thioxanthone in DMSO was excited at 266 nm, and its fluorescence emission (390–500 nm) was spectrally integrated. The fluorescence lifetime of thioxanthone in DMSO is 140 ps,[40] which is significantly shorter than the expected time resolution of the experiment. Consequently, its contribution to the IRF is negligible. The finite time resolution was accounted for by convolution with a Gaussian function representing the IRF with a FWHM of ~7 (NMA) and ~10 ns (NMA-dF, NMA-OMeF and NMA-dOMe).

Synthesis of the acridones

2,7-Difluoro-10-methylacridin-9(10*H*)-one (NMA-dF) was prepared by Ullmann-type coupling from 4-fluoro-aniline and 2-bromo-5-fluoro-benzoic acid, followed by intramolecular Friedel–Crafts acylation to give 2,7-difluoroacridin-9(10*H*)-one and final *N*-methylation.[2] 5-Fluoro-2-((4-methoxyphenyl)amino)benzoic acid was prepared by Ullmann-type coupling from 4-methoxyaniline and 2-bromo-5-fluorobenzoic acid following literature procedure.[41] The cyclization to the acridone was done *via* a modified procedure by Kelly *et al.*[42] using methanesulfonic acid. 2-Fluoro-7-methoxy-10-methylacridin-9(10*H*)-one (NMA-OMeF) was prepared by final methylation[43] (see ESI†). 2,7-Dimethoxy-10-methylacridin-9(10*H*)-one (NMA-dOMe) was prepared by Ullmann-type coupling from 2-bromo-5-methoxybenzoic acid and 4-methoxyaniline, followed by intramolecular Friedel–Crafts acylation to give 2,7-dimethoxyacridin-9(10*H*)-one and final *N*-methylation.[42,44–46] The purity of the acridones was verified by ^{1}H-, ^{13}C and ^{1}F-NMR spectroscopy (see ESI,† Fig. S1–S10).

Sample preparation

NMA (≥98.0%) and DCB (≥99.0%) were obtained from TCI. THF (≥99.9%) and ethanol (HPLC) were purchased from Sigma Aldrich. Coumarin 102 was purchased from Radiant Dyes Laser & Acc. All measurements were performed at room temperature (~20 °C). To deoxygenate sample solutions, nitrogen (Air Liquide, 99.999%) or argon (Air Liquide, 99.999%) were bubbled through. Gases were saturated with the solvent to reduce concentration changes. All chemicals obtained commercially were used as received.

Quantum chemical calculations

Geometry optimizations were conducted with the Gaussian 16 program[47] using density functional theory (DFT) with the PBE0 functional for the ground state and time-dependent DFT (TDDFT) for the excited states, additionally applying the Tamm–Dancoff approximation (TDDFT-TDA) in the triplet manifold. The Ahlrichs def-SVP basis set[48] was used throughout. Computed vibrational frequencies confirmed that all geometries obtained correspond to true minima. Vertical excitation energies at fixed geometries were computed with the DFT/MRCI program.[49] The redesigned Hamiltonian R2016[50] was used with standard parameters and a selection threshold of 1.0 Hartree. The core electrons were kept frozen, the initial reference space comprised all single and double excitations of 10 electrons in 10 orbitals and was subsequently optimized to contain the most important configurations of all roots. For the 0–0 energies, vibrational zero-point energies computed at the (TD)DFT level were added to the DFT/MRCI energies. The solvent was considered implicitly employing the polarizable continuum model.[47] Spin–orbit coupling matrix elements were computed with the SPOCK program in the atomic mean field approximation.[51,52] Nonadiabatic coupling matrix elements (NACMEs) were obtained with the program DELTA.[53] ISC and IC rate constants at a temperature of 293.15 K were computed *via* the generating function approach as implemented in the program VIBES.[53–55]

Results

The absorption band lowest in energy is very similar for all substituted NMAs and NMA dissolved in THF (Fig. 3). All of

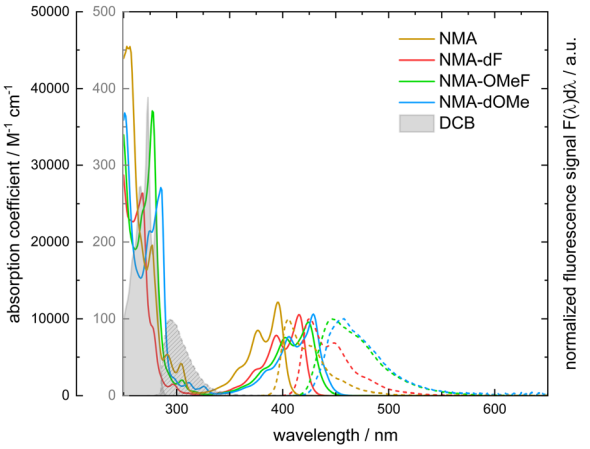

Fig. 3 Absorption coefficient (solid lines) and fluorescence (normalized, dashed lines) spectra of NMA (yellow), NMA-dF (red), NMA-OMeF (green), NMA-dOME (blue) and DCB (grey areas) in THF. The black y-axis on the left refers to absorption coefficients of the NMAs, the gray one to absorption coefficients of DCB. For the acquisition of the fluorescence spectra the excitation was tuned to the absorption maxima lowest in energy.

them feature pronounced vibronic progression with two peaks and a shoulder. Compared to NMA in THF, the absorption of the derivates is bathochromically shifted. The magnitude of this shift increases in the following order: NMA-dF, NMA-OMeF and NMA-dOMe. The absorption of NMA features peaks at 395 nm and 377 nm and a shoulder around 358 nm. NMA-dF features peaks at 415 nm and 394 nm and a shoulder around 374 nm. NMA-OMeF features peaks at 424 nm and 402 nm and a shoulder around 381 nm. NMA-dOMe features peaks at 429 nm and 406 nm and a shoulder around 383 nm. The peak absorption coefficient of NMA at its longest wavelength maximum is around 12 000 M^{-1} cm^{-1}, while the NMA derivatives exhibit a coefficient of around 10 000 M^{-1} cm^{-1}.

Emission takes place in the range between 380 nm to 600 nm (see Fig. 4, left). Compared to NMA, the emission of NMA-dF, NMA-OMeF and NMA-dOMe is bathochromically shifted. The absorption and fluorescence of NMA and NMA-dF obey the mirror image rule.[7] NMA features emission peaks at 405 nm and at 427 nm, resulting in CIE coordinates of (0.16, 0.02). The emission maxima of NMA-dF are located at 425 nm and 449 nm, resulting in CIE coordinates of (0.15, 0.04). For NMA-OMeF and NMA-dOMe the mirror image rule is partially fulfilled. Their emission peak is broadened compared to the absorption, thus obscuring the vibrational progression. Consequently, the emission spectra of NMA-OMeF as well as NMA-dOMe features just one maximum. For NMA-OMeF the maximum appears at 446 nm with CIE coordinates of (0.15, 0.11) and for NMA-dOMe at 457 nm with CIE coordinates of (0.14, 0.12). From the spectra in the transition dipole representation, the 0–0 energy as well as the Stokes shift were obtained. For NMA, a 0–0 energy of 25 000 cm^{-1} (3.10 eV) and a Stokes shift of 560 cm^{-1} (69.4 meV), for NMA-dF a 0–0 energy of 23 800 cm^{-1} (2.95 eV) and a Stokes shift of 570 cm^{-1} (70.7 meV), for NMA-OMeF of 23 100 cm^{-1} (2.86 eV) and of 1500 cm^{-1} (186.0 meV), and for NMA-dOMe of 22 800 cm^{-1} (2.83 eV) and of 1530 cm^{-1} (189.7 meV) were determined. *Via* Strickler–Berg analysis,[33,34] radiative rate constants (k_{rad}) for NMA of 7.43 × 10^7 s^{-1}, for NMA-dF of 6.18 × 10^7 s^{-1}, for NMA-OMeF of 5.42 × 10^7 s^{-1}, and for NMA-dOMe of 5.53 × 10^7 s^{-1} were determined.

The fluorescence quantum yield ϕ_{fl} of NMA, NMA-dF, NMA-OMeF and NMA-dOMe in THF were measured with coumarin 102 (ϕ_{fl} = 0.764 in air-saturated ethanol[30]) as a reference. Yields of 0.11 ± 0.02 and 0.09 ± 0.02 (NMA), 0.68 ± 0.02 and 0.53 ± 0.04 (NMA-dF), 0.79 ± 0.02 and 0.54 ± 0.01 (NMA-OMeF), as well as 0.84 ± 0.05 and 0.53 ± 0.02 (NMA-dOMe) in deoxygenized (DO) and air-saturated (air) solutions were obtained. Fluorescence decays of the samples could be modelled single-exponentially.

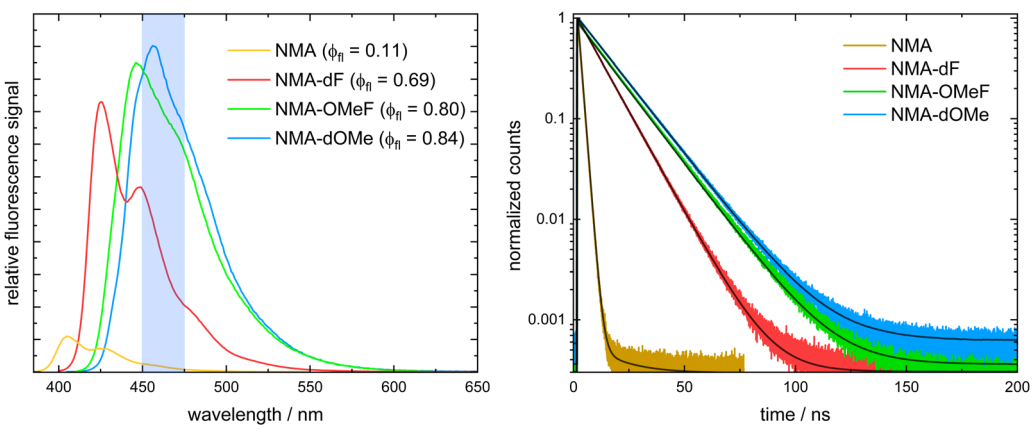

Fig. 4 Fluorescence spectra and fluorescence decay traces for NMA (yellow), NMA-dF (red), NMA-OMeF (green), and NMA-dOMe (blue) dissolved in deoxygenized THF. The sample concentrations ranged from 10^{-6} to 10^{-5} M. Left: Fluorescence spectra. All spectra are scaled such that their integrals match the respective fluorescence quantum yields ϕ_{fl}. The deep blue region is highlighted in blue. The excitation wavelengths were set to 375 nm for NMA, 395 nm for NMA-dF, 405 nm for NMA-OMeF and 410 nm for NMA-dOMe. All spectra were recorded with a resolution of 1 nm. Right: Fluorescence decay traces recorded by TCSPC of the samples. The excitation and detection wavelengths were 375 nm and 405 nm for NMA, 416 nm and 450 nm for NMA-dF, 424 nm and 446 nm for NMA-OMeF and 429 nm and 457 nm for NMA-dOMe. Experimental results are plotted in different colors, the black solid lines represent the fits.

The respective fluorescence lifetimes τ_{fl} were determined by TCSPC to be 1.5 and 1.4 ns (NMA), 10.8 and 8.6 ns (NMA-dF), 14.6 and 10.0 ns (NMA-OMeF) as well as 15.4 and 9.7 ns (NMA-dOMe) in deoxygenized (Fig. 4, right) and air-saturated solutions (Fig. S11, ESI†). The error of these lifetimes is $<\pm 1\%$. The fluorescence lifetimes τ_{fl} measured directly can be compared with ones τ_{fl}^{SB} derived from the radiative rate constant k_{rad} and the fluorescence quantum yield ϕ_{fl} according to eqn (3),

$$\tau_{fl}^{SB} = \frac{\phi_{fl}}{k_{rad}}. \quad (3)$$

Except for NMA, these lifetimes τ_{fl}^{SB} are very close to the ones obtained by TCSPC (*cf.* Table 1). This indicates that steady state and time-resolved measurements are consistent. An equilibrium between the $^1\pi\pi^*$ and $^{1,3}n\pi^*$ states upon optical excitation is disfavored. However, for NMA in THF, τ_{fl}^{SB} and τ^{TCSPC} differ slightly from each other, suggesting that an equilibrium between the $^1\pi\pi^*$ and $^{1,3}n\pi^*$ states is present. For thioxanthone in methanol such equilibration resulted in a reduction of the spectrally integrated stimulated emission (SE) on the picosecond time scale.[56] In respective femtosecond transient absorption experiments (see Fig. S12, ESI†) on the NMA samples, such a reduction was only observed for the unsubstituted NMA (see Fig. 5, note that the SE is a negative signal). The early increase in SE seen for all samples is presumably due to dielectric relaxation.[57] Thereafter, the signals remain constant up to ~1 ns for all samples except NMA. For NMA, a small reduction of the signal on the time scale of 10 ps is observed. A single exponential fit of this time dependence affords the ratio $(I_0 - I_{ep})/I_0$. I_0 is the integrated SE at time zero and I_{eq} the one after equilibration between the two states. As detailed in ref. 56, this ratio equals the equilibrium constant K, see eqn (4),

$$\frac{I_0 - I_{eq}}{I_{eq}} = K = \frac{[^3n\pi^*]}{[^1\pi\pi^*]}. \quad (4)$$

Table 1 Photophysical properties of NMA, NMA-dF, NMA-OMeF, and NMA-dOMe in THF. The absorption (λ_{abs}) and emission (λ_{em}) maxima were obtained from steady state spectroscopy recorded with constant wavelength resolution. The Stokes shifts ($\Delta\tilde{\nu}$) and 0–0-energies (E_{0-0}) given in wavenumbers were deduced relying on the transition dipol moment representation.[32] Radiative rate constants (k_{rad}) were determined using the Strickler–Berg relation. The non-radiative rate constants (k_{nr}) were determined *via* $k_{nr} = \frac{1-\phi_{fl}}{\tau^{TCSPC}}$. The fluorescence quantum yields of air-saturated (ϕ_{fl}^{air}) and deoxygenized (ϕ_{fl}^{DO}) samples were determined relative to the standard C102 in ethanol.[30] Fluorescence lifetimes determined directly by TCPSC (τ^{TCSPC}) and from the rate constants k_{rad} and yields ϕ_{fl}^{DO} (τ^{SB}) are included

Parameters	NMA	NMA-dF	NMA-OMeF	NMA-dOMe
λ_{abs}/nm	396	416	424	429
λ_{em}/nm	405	425	446	457
$\Delta\tilde{\nu}$/cm^{-1}	560	570	1500	1530
E_{0-0}/cm^{-1}	25 000	23 800	23 100	22 800
k_{rad}/s^{-1}	7.79×10^7	6.18×10^7	5.42×10^7	5.53×10^7
k_{nr}/s^{-1}	5.86×10^8	2.96×10^7	1.43×10^7	1.04×10^7
ϕ_{fl}^{air}	0.09	0.53	0.54	0.53
ϕ_{fl}^{DO}	0.11	0.68	0.79	0.84
τ^{SB}/ns	1.36	11.00	14.58	15.19
τ^{TCSPC}/ns	1.52	10.81	14.64	15.41

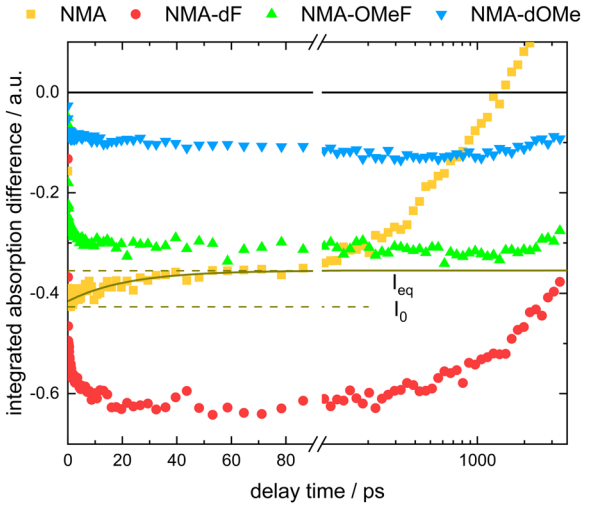

Fig. 5 Decay of the spectrally integrated SE of NMA (yellow), NMA-dF (red), NMA-OMeF (green), and NMA-dOMe (blue) dissolved in THF. The transient absorption spectra were spectrally integrated over the ranges of the SE that do not overlap with the ground state bleach (NMA: 415–460 nm, NMA-dF: 450–500 nm, NMA-OMeF: 455–500 nm, NMA-dOMe: 459–500 nm) to obtain the time traces. For NMA, experimental results are compared to a single-exponential fit and the parameters I_0 and I_{eq} are marked.

K is hereby defined with the $^3n\pi^*$ state as the product of the equilibration. The fit yields a K value of 0.18. A second procedure to determine the constant K relies on the fluorescence spectrum and the transient absorption spectra around time zero and after equilibration. The fluorescence spectrum was converted to a SE spectrum,[58,59] flipped, shifted, and scaled to match the SE contributions (see Fig. S12, ESI†) in the transient absorption spectra. The respective scaling factors were taken to be proportional to I_0 and I_{eq}. This second procedure yields a value (0.15) very close to the first one. This equilibration can also explain the small difference in fluorescence lifetimes measured directly (τ^{TCSPC}) and indirectly (τ^{SB}, see Table 1). In the indirect approach (Strickler Berg and fluorescence quantum yield), the equilibration is not accounted for. The effect can be considered by modifying eqn (3) to eqn (5) (see ref. 56),

$$\tau_{fl}^{corr} = \frac{\Phi_{fl}}{k_{rad}} \cdot (K+1) = \tau^{SB}(K+1). \quad (5)$$

With the constant K equal to 0.15, the corrected lifetime is 1.56 ns which is close to the one measured directly (1.52 ns). Neglecting entropy contributions and assuming that only one triplet sub-level is populated during the equilibration,[60] the constant K can be related to a singlet triplet energy gap ΔE_{ST} using eqn (6),

$$\Delta E_{ST} = -k_B T \cdot \ln K. \quad (6)$$

With a thermal energy at room temperature k_BT, a gap of 350–380 cm^{-1} results (the $^3n\pi^*$ state is above the $^1\pi\pi^*$ one). In addition to the constant K, the fit also yields a time constant of 22 ps for equilibration. The value is close to the time constant reported earlier for thioxanthone in methanol.[56]

All of the four compounds have quantum yields ϕ_{fl} somewhat smaller than one. This suggests that non-radiative processes are competing with the fluorescence emission. By nanosecond transient absorption spectroscopy, the quantum yield of the lowest triplet state ϕ_T of NMA-OMeF in THF was estimated to 0.14 ± 0.02 (Fig. S13, ESI†). Like for NMA-dF in MeOH[2] it was, thus, shown that the non-radiative decay is mostly due to ISC. Due to the similar structures of NMA, NMA-dF and NMA-dOMe, ISC to the T_1 state is expected to be the dominant non-radiative decay channel for these compounds as well.

All three substituted emitters have a high fluorescence quantum yield ϕ_{fl} in an aprotic environment and emit with rate constants k_{rad} larger than 5.4×10^7 s^{-1} in the deep blue wavelength range. However, in order to be suitable as OLED emitters, it must first be determined whether the molecules also convert triplet excitations into light in an aprotic environment.

Through sensitized excitation, the T_n state of the emitter can be accessed if the T_1 state of the sensitizer is higher in energy than the T_n state of the emitter. However, the energies of the T_n states ($^3n\pi^*$) are not accessible experimentally. They are presumably close to the energy of the S_1 states which are in the order of 22 800–25 000 cm^{-1} (2.82–3.10 eV, Table 1). In previous studies employing methanol as a solvent,[1,2] DCB proved useful in this respect. It features a T_1 0–0 energy of 27 990 cm^{-1} (3.47 eV) in the solid state[61] (higher in energy than the S_1 states of all NMAs) and a high triplet quantum yield in methanol solution (ϕ_T^{MeOH} = 0.96).[62] However, the triplet quantum yield of DCB in THF is not known. It is assumed that due to its symmetrical nonpolar nature, the molecule interacts only weakly with its surroundings, resulting in the energy of states remaining nearly unchanged. A comparison of fsTA measurements of DCB in methanol and in THF reveals that the spectral signatures are very similar in the two solvents. DCB in THF, photo-excited at 266 nm, exhibits a time constant of 625 ps (Fig. S14, ESI†) compared to 550 ps reported for DCB in MeOH.[1] The time constant is assigned to the S_1 decay of DCB and the concomitant population of its T_1 state. An estimate of the triplet quantum yield of DCB in THF ϕ_T^{THF} is conducted by comparing the transient absorption at time zero due to the S_1 (ΔA_{S_1}) and the transient absorption of the triplet state (ΔA_{T_1}) at ~3.1 ns, when only the T_1 state contributes to the signal. This determination of the yield ϕ_T^{THF} rests on the assumption that the difference absorption coefficients of S_1 and T_1 states are not affected by the solvent. This assumption is supported by the observation that the absorption spectra exhibit only minor changes in the ground state.[1] The triplet quantum yield was calculated using eqn (7),

$$\phi_T^{THF} = \phi_T^{MeOH} \cdot \frac{\Delta A_{T_1}^{THF} \cdot \Delta A_{S_1}^{MeOH}}{\Delta A_{T_1}^{MeOH} \cdot \Delta A_{S_1}^{THF}}. \quad (7)$$

The triplet yield ϕ_T^{MeOH} was reported to be 0.95.[62] The procedure affords a yield ϕ_T^{THF} of 0.76 which is slightly lower than the one in methanol.

For the sensitization experiment, deoxygenated solutions containing DCB and the NMAs were excited using 266 nm laser pulses, which corresponds to the lowest energy absorption of DCB. An exclusive excitation of the sensitizer is not possible because the absorption band of DCB overlaps with higher absorption bands of the emitters (*cf.* Fig. 3). With a gated CCD camera, the emission of the NMAs induced by the laser was monitored. The fluorescence emission of DCB and all NMAs are spectrally well separated (*cf.* Fig. 3). The time dependence of the NMAs emission was characterized based on spectral integrals. These cover the range of the NMAs steady state emissions. The resulting time traces were plotted using a log–log representation (Fig. 6). For all the NMAs studied, in absence of DCB, a decay on the 1–10 ns time scale as well as one with a characteristic time of ~1 μs is observed. The latter one, has an amplitude three orders of magnitude smaller than the first one. Spectral signatures of both components match the ones of steady state fluorescence spectroscopy. A single exponential fit of the prompt fluorescence decay accounting for the instrumental response time (~10 ns) yields time constants of 2.49 ± 0.08 ns for NMA, 11.1 ± 0.02 ns for NMA-dF, 14.5 ± 0.15 ns for NMA-OMeF and 16.1 ± 0.01 ns for NMA-dOMe. These time constants for the substituted NMAs are in very good agreement with the TCSPC results discussed earlier. Minor discrepancies can be explained by the long IRF time (~10 ns) compared to the observed decay time. Fits of the second decay component afforded lifetimes of 726 ± 26 ns for NMA, 877 ± 13 ns for NMA-dF, 1056 ± 31 ns for NMA-OMeF and 1780 ± 55 ns for NMA-dOMe. Following the reasoning for thioxanthone[1] and NMA-dF in methanol,[2] this decay component is assigned to triplet–triplet annihilation (TTA). In the weak depletion limit,[63] the time constant τ_{TTA} determined *via* time-resolved fluorescence spectroscopy ought to be half of the respective triplet lifetime τ_T, *i.e.* $\tau_{TTA} = \frac{\tau_T}{2}$.[63] For an exemplary NMA (NMA-OMeF), the triplet lifetime τ_T was determined by nanosecond transient absorption measurements. The measurement afforded an intrinsic decay of $k_0^{NMA\text{-}OMeF}$ = $5.39 \times 10^5 \pm 1.38 \times 10^4$ s^{-1} and a self-quenching constant of $k_q^{NMA\text{-}OMeF}$ = $6.38 \times 10^8 \pm 1.09 \times 10^8$ M^{-1} s^{-1} (*cf.* Fig. S15, left, ESI†). For the concentration employed in the sensitization experiment (0.29 mM), this translates into a lifetime τ_T of 1.38 ± 0.1 μs. From the lifetime τ_{TTA} one would expect a similar triplet lifetime τ_T of 2.1 ± 0.06 μs. Presumably, the triplet lifetime τ_T deduced from the nanosecond transient absorption measurements is more reliable since more data points contribute to its evaluation.

The addition of DCB to the solutions results in a decrease of the initial emission signal. This is expected because less emitter molecules are excited due to the inner filter effect of DCB. For NMA, no significant differences from 10 ns onwards are observed. The observation that the signal levels after ~10 ns are very similar suggests that triplet energy transfer between DCB and NMA occurs and is followed by TTA. For the NMA derivates, stronger signals from ~100 ns until ~1000 ns are observed in presence of DCB compared to emitter only measurements. The emission spectra observed during that period are identical to the ones for prompt fluorescence (Fig. S16, ESI†). This gives clear-cut evidence for an energy transfer (EET) between excited DCB and the NMAs. The time scale of this EET

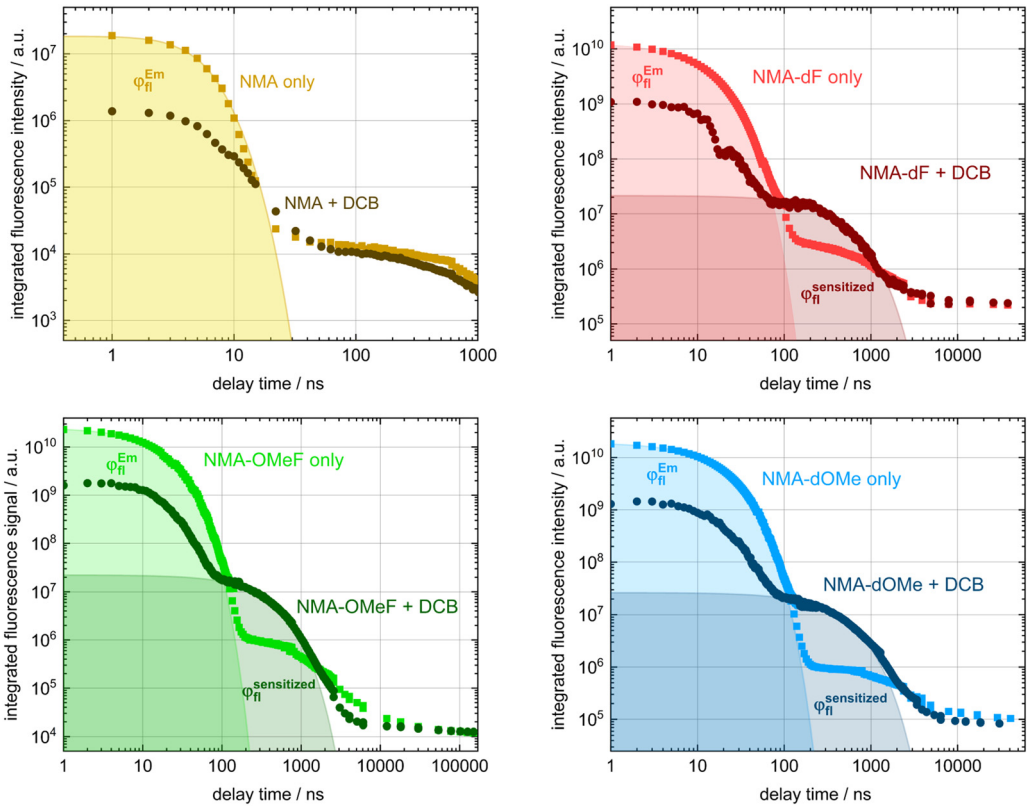

Fig. 6 Comparison of direct (emitter only) and sensitized (DCB present) excitation of NMA derivatives dissolved in THF. Sample solutions were excited with 266 nm laser pulses and the emission traced as a function of time with a gated CCD. The spectrally integrated emission (380–650 nm) of each emitter (NMA in yellow, NMA-dF in red, NMA-OMeF in green and NMA-dOMe in blue) was plotted *versus* the delay time. Note the log–log representation. The brighter points represent the measured values of the emitter (0.27–0.29 mM) only solution, while the darker ones depict the behavior after the addition of DCB (0.27–0.29 M). The shaded regions beneath the solid lines are proportional to the quantum yields φ_{fl}^{Em} and $\varphi_{fl}^{Sensitized}$, from which the efficiency η is determined.

excludes a singlet–singlet mechanism as the DCB S_1 lifetime amounts to only 625 ps in THF. Therefore, the triplet states of DCB have to be involved in the EET. Single exponential fits of the additional components afforded time constants (τ_{Sens}) of 420 ± 8 ns for NMA-dF, 321 ± 2 ns for NMA-OMeF and 407 ± 3 ns for NMA-dOMe. At even longer delay times the decay matches the TTA from the emitter only solutions. There are no signs for an enhanced TTA due to the energy transfer.

The measured time constants τ_{Sens} ought to relate to rate constants according to eqn (8),

$$\frac{1}{\tau_{Sens}} = k_0^{Sens} + k_q[\text{emitter}]. \quad (8)$$

The intrinsic decay constant of the T_1 state of DCB k_0^{Sens} was determined to be $1.48 \times 10^6 \pm 7.3 \times 10^3\ s^{-1}$ $\left(\triangleq 0.7\ \mu s\right)$ *via* nanosecond transient absorption spectroscopy. Like in methanol,[2] DCB in THF exhibits no significant concentration quenching (Fig. S15, right, ESI†). Using the time constants τ_{Sens} determined from the results in Fig. 6 and eqn (8) the following quenching constants k_q result: $k_q^{NMA\text{-}dF} = 3.31 \times 10^9\ M^{-1}\ s^{-1}$, $k_q^{NMA\text{-}OMeF} = 5.65 \times 10^9\ M^{-1}\ s^{-1}$, and $k_q^{NMA\text{-}dOMe} = 3.40 \times 10^9\ M^{-1}\ s^{-1}$. The experimentally determined values are close to the diffusion-limited rate constant ($1.3 \times 10^{10}\ M^{-1}\ s^{-1}$ in THF[28]). The efficiency $\eta \leq 1$ for the transfer of DCB triplet excitation to emitted NMA photons can be evaluated following a procedure detailed in ref. 2. The procedure requires the fluorescence quantum yields for direct (φ_{fl}^{Em}) and sensitized excitation ($\varphi_{fl}^{Sensitized}$), as well as the fraction of excitation light absorbed by the emitter and the sensitizer. The quantum yields φ_{fl}^{Em} and $\varphi_{fl}^{Sensitized}$ are proportional to the areas marked in Fig. 6. The procedure results in an efficiency of $\eta^{NMA-dF} = 0.070$, $\eta^{NMA-OMeF} = 0.022$ and $\eta^{NMA-dOMe} = 0.037$. By considering the triplet quantum yield ($\phi_T^{THF} = 0.76$), the intrinsic decay constant of the T_1 state of DCB k_0^{Sens} in THF, and the quenching constant times the corresponding emitter concentration, k_q[Emitter], a transfer efficiency η_∞ can be calculated. The efficiency η_∞ quantifies the fraction of quenching events resulting in an S_1 excitation of the emitter for an infinitely high emitter concentration. This efficiency amounts to $\eta_\infty^{NMA-dF} = 0.243$, $\eta_\infty^{NMA-OMeF} = 0.055$, and $\eta_\infty^{NMA-dOMe} = 0.122$.

Quantum chemical computations on NMA, NMA-dF, NMA-OMeF, and NMA-dOMe in THF support the experimental results. The computations place the 0–0-energy of the S_1 state ($^1\pi\pi^*$) for NMA at 25 700 cm^{-1} (3.19 eV), NMA-dF at 24 600 cm^{-1} (3.05 eV), NMA-OMeF at 24 000 cm^{-1} (2.98 eV) and for NMA-dOMe at 22 800 cm^{-1} (2.83 eV). Radiative rate constants of $k_{rad}^{NMA} = 6.98 \times 10^7\ s^{-1}$ (oscillator strength of 0.15816),

Table 2 Calculated adiabatic and 0–0-energies of the states in THF

	Energies/ cm^{-1}	S_1 ($^1\pi\pi^*$)	S_2 ($^1n\pi^*$)	T_1 ($^3\pi\pi^*$)	T_2 ($^3n\pi^*$)	T_3 ($^3\pi\pi^*$)
NMA	Adiabatic	26 700	26 900	21 500	25 700	
	0–0	25 700	26 100	20 600	25 000	
NMA-dF	Adiabatic	25 500	26 500	19 900	25 300	
	0–0	24 600	25 800	19 100	24 600	
NMA-OMeF	Adiabatic	24 800	26 900	19 000	25 600	
	0–0	24 000	26 100	18 400	24 900	
NMA-dOMe	Adiabatic	23 600	26 800	18 100	25 600	26 100
	0–0	22 800	26 100	17 500	24 700	24 900

k_{rad}^{NMA-dF} = 6.90 × 10^7 s^{-1} (oscillator strength of 0.17209), $k_{rad}^{NMA-OMeF}$ = 6.24 × 10^7 s^{-1} (oscillator strength of 0.16804) and $k_{rad}^{NMA-dOMe}$ = 5.56 × 10^7 s^{-1} (oscillator strength of 0.16251) were computed. All those computed values are in good agreement with the experimental ones (*cf.* Tables 1 and 2). The 0–0-energy of the T_1 state ($^3\pi\pi^*$) are calculated to be 20 600 cm^{-1} (2.55 eV) for NMA, 19 100 cm^{-1} (2.37 eV) for NMA-dF, 18 400 cm^{-1} (2.28 eV) for NMA-OMeF, and 17 500 cm^{-1} (2.17 eV) for NMA-dOMe. The energy gaps between the bright S_1 states and the T_1 states are of the order of ~5300 cm^{-1} (0.66 eV) excluding a role of the T_1 state in thermally activated delayed fluorescence. All the NMAs feature an upper triplet state T_n with $^3n\pi^*$ character which is close in energy to the S_1 state ($^1\pi\pi^*$). While the energies of the $\pi\pi^*$ states are lowered by up to ~3000 cm^{-1} (0.37 eV) by the introduction of the substituents, the energies of the $n\pi^*$ states remain almost constant. For the vertical excitation energies at different geometries, see Tables S2–S5 (ESI†). The associated molecular orbitals are shown in Fig. S17–S20 (ESI†).

All T_n (n = 2) energies are smaller than 27 987 cm^{-1} (3.47 eV, triplet energy of DCB[61]) indicating that EET from DCB is energetically feasible. Once the T_n (n = 2) state is populated, for HIGHrISC to be relevant, the rate constants of the rISC process (k_{rISC}) must be at least of a similar magnitude as the rate constants of the competing $T_2 \rightarrow T_1$ IC process (k_{IC}). Thus, the relevant rate constants were computed using the generating function approach,[54,55] the results are compiled in Table 3. The spin–orbit coupling (SOC) matrix elements entering the expression for the (r)ISC rate constants are in the range of ~10 to 17 cm^{-1}. This is substantially lower than the value of 154 cm^{-1} for atomic oxygen.[28] The oxygen atom of the carbonyl moiety is mostly responsible for the SOC. As other atoms contribute to the relevant MOs (n and π*), its contribution is "diluted".[64] For all compounds, except NMA, rate constants for rISC and IC of the order of 10^{10}–10^{11} s^{-1} were calculated. For, *e.g.*, NMA-dOMe, the rate constant of rISC is by a factor of 3.8 higher than the one of IC. So, according to this computation rISC is favored over IC in NMA-dOMe. However, for a proper interpretation of the results, the (small) discrepancies between experimental and computational excited state energies need to be considered (see Discussion).

Table 3 Calculated rate constants of the rISC, ISC and IC between the relevant states of the NMAs in THF

Rate constants/s^{-1}	NMA	NMA-dF	NMA-OMeF	NMA-dOMe
k_{rISC} $^3n\pi^* \rightarrow {}^1\pi\pi^*$	1.30 × 10^9	8.80 × 10^{10}	4.80 × 10^{10}	5.08 × 10^{10}
k_{ISC} $^1\pi\pi^* \rightarrow {}^3n\pi^*$	3.18 × 10^{10}	7.49 × 10^{10}	4.85 × 10^8	1.51 × 10^6
k_{IC} $^3n\pi^* \rightarrow {}^3\pi\pi^*$	2.61 × 10^{11}	6.45 × 10^{10}	3.67 × 10^{10}	1.35 × 10^{10}

Discussion

As the orbital diagrams in Fig. 1 suggest, decorating NMA at position 2 and/or 7 with +M substituents lowers the $^1\pi\pi^*$ excitation energies. In steady state spectroscopy, red shifts of 0–0 energies of up to ~2200 cm^{-1} (0.27 eV) are observed (*cf.* Table 1 and Fig. 3). The trend in 0–0 energies inferred from spectroscopy is well reproduced by quantum chemistry (*cf.* Tables 1 and 2). The lowering of the $^1\pi\pi^*$ state shifts the emission of the substituted NMAs to the deep blue region. The L'Eclairage (CIE) coordinates of all emitters are located at the bottom left of the CIE chromaticity diagram (*cf.* Fig. 7). The CIE coordinates of the NMAs are already close to the one of the standard for deep blue emitters (0.14, 0.08) as set by the National Television System Committee (NTSC 1987).[26] However, it is important to note that the CIE coordinates of the emitters were determined in solution and not in an OLED.

The reduction of the $^1\pi\pi^*$ energy goes along with a substantial increase of the fluorescence quantum yield ϕ_{fl}. For NMA a value of 0.11 was determined, for NMA-dOMe it is as high as 0.84 (*cf.* Fig. 4). This indicates that non-radiative decay channels involving $n\pi^*$ states are suppressed. The quantum chemical computations corroborate this trend. In the computations, +M substitutions at positions 2 and 7 leave $n\pi^*$energies essentially untouched (*cf.* Fig. 8, red circles). This finding is in line with a qualitative consideration based on the molecular orbitals (*cf.* Fig. 1). The π*-orbital of NMA has nodes at these positions and the n-orbital features no electron density here. As the $n\pi^*$ states retain their energies upon substitution and $\pi\pi^*$ states are lowered, for all substituted derivatives studied, the $^1\pi\pi^*$ state is below the $^{1,3}n\pi^*$ ones. Accordingly, the

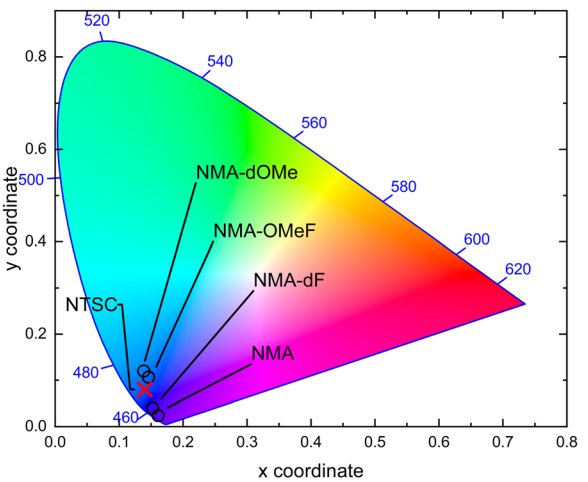

Fig. 7 CIE chromaticity diagram with the CIE coordinates of the emission of NMA (0.16, 0.02), NMA-dF (0.15, 0.04), NMA-OMeF (0.15, 0.11), and NMA-dOMe (0.14, 0.12) in THF. The CIE coordinate of the standard deep blue emitter (0.14, 0.08) set by the National Television System Committee (NTSC) is marked with a red cross.

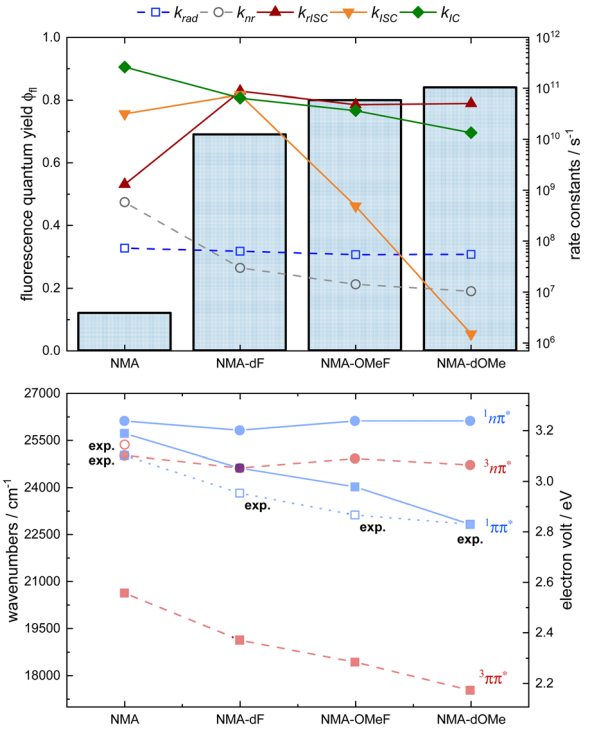

Fig. 8 Fluorescence quantum yields, experimentally determined rate constants (k_{rad}, k_{nr}, open symbols) as well as calculated rate constants (k_{rISC}, k_{ISC}, k_{IC}, filled symbols), and quantum chemical/experimental 0–0 energies given in cm^{-1} and eV of the NMAs in THF. Top: Fluorescence quantum yields ϕ_{fl} (bar chart), k_{rad} (blue open squares), k_{nr} (grey open circles), k_{rISC} (red triangles), k_{ISC} (orange triangles), and k_{IC} (green diamonds) of the NMAs in THF. Note the log representation for the rate constants. Bottom: Calculated and experimentally determined 0–0 energies of the NMAs in THF. Singlet states are represented in blue, triplet states in red, ππ* states are shown as squares, nπ* states as circles. The blue open squares represent the experimentally determined 0–0 energies (exp.) of the S_1 states. The red open circle represents the experimentally determined energy of the T_2 state (^{3}nπ*) of NMA.

fluorescence quantum yields ϕ_{fl} increase and the non-radiative rate constants decrease (*cf.* Table 1 and Fig. 8).

However, according to the quantum chemistry for NMA, the ^{1}nπ* state is seen to be 400 cm^{-1} above the ^{1}ππ* one and the ^{3}nπ* – 700 cm^{-1} below this state (see Fig. 8). The experiment suggests that the computation places the nπ* energies slightly too low. The analysis of the early SE decay (*cf.* Fig. 5) places the ^{3}nπ* state slightly (by 350–380 cm^{-1}) above the ^{1}ππ* one. Due to this discrepancy, the computation predicts a small fluorescence quantum yield $\phi_{fl}\left(\approx \frac{k_{rad}}{k_{rad}+k_{ISC}}\right)$ of 0.003 instead of the measured 0.11. Interestingly, measured and calculated time constants τ_{eq} for the equilibration between the S_1 and the T_2 state are very close despite this discrepancy. The value of τ_{eq} derived from the computed rate constants *via* $\tau_{eq} = \frac{1}{k_{rISC}+k_{ISC}}$[65] amounts to 30 ps which compares very favorably with the experimental value of 22 ps. As shown in the ESI† (Fig. S21), for small values of the energy gap $\Delta E_{S_1T_2}$, the time constant τ_{eq} is rather insensitive to $\Delta E_{S_1T_2}$. As one shifts the T_2 state from small energies towards the S_1 state, the rate constant k_{ISC} decreases and the rate constant k_{rISC} increases leaving $k_{ISC} + k_{rISC}$ and thereby τ_{eq} nearly constant. The calculated rate constants suggest a rapid equilibration between the S_1 state and T_2 state for all NMAs. For the substituted NMAs, however, no early decay of the SE traces is discernible suggesting that the ^{3}nπ* states are too high in energy for a detectable depletion of the ^{1}ππ* state due to equilibration. The small equilibrium population of the ^{3}nπ* state in the derivatives renders IC from ^{3}nπ* to ^{3}ππ* state inefficient. All this indicates that the substitutions – particularly by methoxy groups – turn NMA also in an aprotic environment into an excellent singlet emitter.

Of course, for OLED applications an emitter should also "process" triplet excitations. The sensibilization experiments give clear evidence that in all substituted NMA derivatives, HIGHrISC is operative. Triplet excited DCB was shown to transfer excitation energy to the studied acridones. This transfer results in an additional fluorescence emission. Thus, rISC from an NMA triplet to the ^{1}ππ* state has to occur. As the lowest triplet state (^{3}ππ*) of all NMAs is by more than −5000 cm^{-1} (−0.6 eV) lower in energy than the ^{1}ππ* state (*cf.* Table 2), the El-Sayed-forbidden rISC from this state can be ruled out safely. This implies that rISC from a higher triplet state (^{3}nπ*) – HIGHrISC is operative. The efficiencies η_∞ = 0.24, 0.06, and 0.12 for this process are below one.

Two loss channels are conceivable (see also discussion in ref. 2). (i) During the EET between triplet excited DCB and the NMAs, instead of a selective population of the ^{3}nπ* state, competing transfer to the ^{3}ππ* could be possible. At present, we do not see an experimental approach to quantify the ratio of the EET processes. A computational study by Penfold *et al.*[66] (on thioxanthone and DCB) has shown that the electronic couplings favor an EET to the T_1 (^{3}ππ*) state over an EET to the T_2 (^{3}nπ*) state. This was attributed to the more delocalized character of the molecular orbitals in the former case. In contrast, the Franck–Condon weighted density of states approximated by a Marcus expression can facilitate the transfer to the T_2 state. The substituted NMAs feature lower ^{3}ππ* energies than NMA itself. Therefore, the transfer to the T_1 state is expected to lie in the Marcus-inverted region[66] which lowers its rate constant. Concomitantly, the efficiency for an EET to the ^{3}nπ* state should rise. Thus, a sizable population of the T_2 state or even its preferential population is plausible. (ii) Alternatively, the loss could be due to an IC process between the ^{3}nπ* and the ^{3}ππ* state competing with the rISC transition (see Fig. 1). For NMA the computations suggest that k_{IC} is two orders of magnitude larger than k_{rISC} (Fig. 8). This could explain the absence of the component τ_{Sens} in the experiment on NMA (see Fig. 6). For the substituted NMAs the increase of the energy gap (ΔE_{TT}) between the T_2 state and T_1 state leads to a decrease of k_{IC} (Fig. 8). The behavior is in line with the energy gap law[7,67] and/or a Marcus inverted behavior.[68] The rate constants k_{rISC} and k_{IC} have the same order of magnitude and both processes can compete with each other. Quantum chemical computations on NMA-dF in methanol[2] suggest that both loss mechanisms ((i) and (ii)) might be operative. Regardless of the exact nature

of the loss channels, the calculations support the assignment of the experimentally observed sensitized emission to HIGHrISC.

Conclusion

This study has shown that the parent compound NMA is not a suitable OLED emitter due to its low fluorescence quantum yield and inability to convert triplet excitons into light in an aprotic environment (such as THF solution). Regarding the use of NMA-dF, NMA-OMeF and NMA-dOMe as deep blue emitters in an OLED, this study has shown that these chromophores can convert both singlet and triplet excitons into light. If the substituted NMA derivative receives energy from a singlet-correlated electron–hole pair, its S_1 state efficiently emits photons with a high fluorescence quantum yield (ϕ_{fl} = 0.7–0.84) and a short fluorescence lifetime ($\tau \approx$ 11–15 ns). If energy is transferred from a triplet-correlated electron–hole pair, resulting in the population of T_n states, the excitons are converted into photons *via* rISC from the T_n to the emissive S_1 state. However, if the excitation reaches the T_1 state, the energy is lost. If the triplet energy is transferred from the host to the emitter by a triplet–triplet energy transfer (as described in ref. 69), the success of the HIGHrISC emitter depends on the choice of a suitable host. The host should be therefore designed in such a way that a predominant transition to the T_n state is achieved.

Author contributions

Matthias Jantz, David Klaverkamp conceived, designed, conducted, and analyzed the experiments. Lennart Bunnemann helped design the structural motive of NMA-OMeF and NMA-dOMe. Furthermore, he performed the synthesis and characterization of NMA-OMeF and NMA-dOMe. Martin Kleinschmidt conducted the quantum chemical calculations. Constantin Czekelius synthesized and characterized NMA-dF. Constantin Czekelius and Peter Gilch did the conceptualization, supervision, funding acquisition, composition, and editing of the manuscript together.

Data availability

The data that supports the findings of this study are available from the corresponding author upon reasonable request.

Conflicts of interest

There are no conflicts of interest to declare.

Acknowledgements

Financial support by the Deutsche Forschungsgemeinschaft (396890929/GRK2482, ''ModISC'') is gratefully acknowledged. Matthias Jantz and David Klaverkamp are grateful for Kekulé scholarships donated by the Fonds der Chemischen Industrie. Thanks to the CeMSA@HHU (Center for Molecular and Structural Analytics @ Heinrich Heine University) for recording the NMR-spectroscopic data. We thank our former bachelor, and master students Lea Hülsmann, Elias Sentob, and Vivienne Laureen Wuttke for their experimental support.

References

1 C. Torres Ziegenbein, S. Fröbel, M. Glöß, R. S. Nobuyasu, P. Data, A. Monkman and P. Gilch, *ChemPhysChem*, 2017, **18**, 2314–2317.
2 K. A. Thom, F. Wieser, K. Diestelhorst, A. Reiffers, C. Czekelius, M. Kleinschmidt, M. Bracker, C. M. Marian and P. Gilch, *J. Phys. Chem. Lett.*, 2021, **12**, 5703–5709.
3 Y. Pan, W. Li, S. Zhang, L. Yao, C. Gu, H. Xu, B. Yang and Y. Ma, *Adv. Opt. Mater.*, 2014, **2**, 510–515.
4 Y. Xu, P. Xu, D. Hu and Y. Ma, *Chem. Soc. Rev.*, 2021, **50**, 1030–1069.
5 J. Wang, A. Chepelianskii, F. Gao and N. C. Greenham, *Nat. Commun.*, 2012, **3**, 1191.
6 M. El-Sayed, *J. Chem. Phys.*, 1963, **38**, 2834–2838.
7 P. Klán and J. Wirz, *Photochemistry of organic compounds: from concepts to practice*, John Wiley & Sons, 2009.
8 B. Heinz, B. Schmidt, C. Root, H. Satzger, F. Milota, B. Fierz, T. Kiefhaber, W. Zinth and P. Gilch, *Phys. Chem. Chem. Phys.*, 2006, **8**, 3432–3439.
9 M. Siegmund and J. Bendig, *Berichte der Bunsengesellschaft für physikalische Chemie*, 1978, **82**, 1061–1068.
10 J. Meissner, B. Kosper, C. M. Marian and R. Weinkauf, *J. Phys. Chem. A*, 2021, **125**, 8777–8790.
11 R. Mundt, T. Villnow, C. T. Ziegenbein, P. Gilch, C. Marian and V. Rai-Constapel, *Phys. Chem. Chem. Phys.*, 2016, **18**, 6637–6647.
12 M. El-Sayed, *J. Chem. Phys.*, 1964, **41**, 2462–2467.
13 T. J. Penfold, E. Gindensperger, C. Daniel and C. M. Marian, *Chem. Rev.*, 2018, **118**, 6975–7025.
14 V. Rai-Constapel and C. M. Marian, *RSC Adv.*, 2016, **6**, 18530–18537.
15 M. Lv, X. Wang, H. Pan and J. Chen, *J. Phys. Chem. B*, 2021, **125**, 13291–13297.
16 M. Siegmund and J. Bendig, *Z. Naturforsch., A*, 1980, **35**, 1076–1086.
17 M. Ito, K. Inuzuka and S. Imanishi, *J. Am. Chem. Soc.*, 1960, **82**, 1317–1322.
18 T. Haldar and S. Bagchi, *J. Phys. Chem. Lett.*, 2016, **7**, 2270–2275.
19 K. A. Thom, *PhD thesis*, Heinrich-Heine-Universität Düsseldorf, 2021.
20 M. Y. Wong and E. Zysman-Colman, *Adv. Mater.*, 2017, **29**, 1605444.
21 T. Chatterjee and K. T. Wong, *Adv. Opt. Mater.*, 2019, **7**, 1800565.
22 F. Rodella, R. Saxena, S. Bagnich, D. Banevičius, G. Kreiza, S. Athanasopoulos, S. Juršėnas, K. Kazlauskas, A. Köhler and P. Strohriegl, *J. Mater. Chem. C*, 2021, **9**, 17471–17482.
23 D. Streets and G. P. Ceasar, *Mol. Phys.*, 1973, **26**, 1037–1052.

24 B. Milián Medina, D. Beljonne, H.-J. Egelhaaf and J. Gierschner, *J. Chem. Phys.*, 2007, **126**, 111101.
25 S. Abou-Hatab, V. A. Spata and S. Matsika, *J. Phys. Chem. A*, 2017, **121**, 1213–1222.
26 D. R. W. G. Hunt, *The N.T.S.C. and Similar Systems of Colour Television*, 2004.
27 M. B. Smith, *March's Advanced Organic Chemistry: Reactions, Mechanisms, and Structure*, John Wiley & Sons, 2020.
28 M. Montalti, A. Credi, L. Prodi and M. T. Gandolfi, *Handbook of Photochemistry*, CRC Press, Boca Raton, 2006.
29 E. Skuodis, O. Bezvikonnyi, A. Tomkeviciene, D. Volyniuk, V. Mimaite, A. Lazauskas, A. Bucinskas, R. Keruckiene, G. Sini and J. V. Grazulevicius, *Org. Electron.*, 2018, **63**, 29–40.
30 K. Rurack and M. Spieles, *Anal. Chem.*, 2011, **83**, 1232–1242.
31 J. Lakowicz, *Principles of fluorescence spectroscopy*, Springer, New York, 2006.
32 G. Angulo, G. Grampp and A. Rosspeintner, *Spectrochim. Acta, Part A*, 2006, **65**, 727–731.
33 S. J. Strickler and R. A. Berg, *J. Chem. Phys.*, 1962, **37**, 814–822.
34 W. W. Parson, *Modern optical spectroscopy*, Springer, Berlin, 2007.
35 W. R. Roberts, T. N. Rohrabaugh and R. M. O'Donnell, *J. Visualized Exp.*, 2021, e62425.
36 S. Fröbel, L. Buschhaus, T. Villnow, O. Weingart and P. Gilch, *Phys. Chem. Chem. Phys.*, 2015, **17**, 376–386.
37 M. Lorenc, M. Ziolek, R. Naskrecki, J. Karolczak, J. Kubicki and A. Maciejewski, *Appl. Phys. B*, 2002, **74**, 19–27.
38 H. Satzger and W. Zinth, *Chem. Phys.*, 2003, **295**, 287–295.
39 T.-O. Peulen, O. Opanasyuk and C. A. Seidel, *J. Phys. Chem. B*, 2017, **121**, 8211–8241.
40 T. Villnow, *PhD thesis*, Heinrich-Heine-Universität Düsseldorf, 2015.
41 T. Jones, N. Monakhova, F. Guivel-Benhassine, A. Lepioshkin, T. Bruel, T. R. Lane, O. Schwartz, A. C. Puhl, V. Makarov and S. Ekins, *ACS Omega*, 2023, **8**, 40817–40822.
42 P. Kancharla, R. A. Dodean, Y. Li, S. Pou, B. Pybus, V. Melendez, L. Read, C. E. Bane, B. Vesely, M. Kreishman-Deitrick, C. Black, Q. Li, R. Sciotti, R. Olmeda, T.-L. Luong, H. Gaona, B. Potter, J. Sousa, S. Marcsisin and J. Kelly, *J. Med. Chem.*, 2020, **63**, 6179–6202.
43 Y. Maegawa, N. Mizoshita, T. Tani and S. Inagaki, *J. Mater. Chem.*, 2010, **20**, 4399–4403.
44 A. Joshi-Pangu, F. Lévesque, H. G. Roth, S. F. Oliver, L.-C. Campeau, D. Nicewicz and D. A. DiRocco, *J. Org. Chem.*, 2016, **81**, 7244–7249.
45 E. Hamzehpoor, C. Ruchlin, Y. Tao, J. E. Ramos-Sanchez, H. M. Titi, G. Cosa and D. F. Perepichka, *J. Phys. Chem. Lett.*, 2021, **12**, 6431–6438.
46 A. Vichet, A.-M. Patellis, J.-P. Galy, A.-M. Galy, J. Barbe and J. Elguero, *J. Org. Chem.*, 1994, **59**, 5156–5161.
47 M. J. Frisch, G. W. Trucks, H. B. Schlegel, G. E. Scuseria, M. A. Robb, J. R. Cheeseman, G. Scalmani, V. Barone, G. A. Petersson, H. Nakatsuji, X. Li, M. Caricato, A. V. Marenich, J. Bloino, B. G. Janesko, R. Gomperts, B. Mennucci, H. P. Hratchian, J. V. Ortiz, A. F. Izmaylov, J. L. Sonnenberg, Williams, F. Ding, F. Lipparini, F. Egidi, J. Goings, B. Peng, A. Petrone, T. Henderson, D. Ranasinghe, V. G. Zakrzewski, J. Gao, N. Rega, G. Zheng, W. Liang, M. Hada, M. Ehara, K. Toyota, R. Fukuda, J. Hasegawa, M. Ishida, T. Nakajima, Y. Honda, O. Kitao, H. Nakai, T. Vreven, K. Throssell, J. A. Montgomery Jr., J. E. Peralta, F. Ogliaro, M. J. Bearpark, J. J. Heyd, E. N. Brothers, K. N. Kudin, V. N. Staroverov, T. A. Keith, R. Kobayashi, J. Normand, K. Raghavachari, A. P. Rendell, J. C. Burant, S. S. Iyengar, J. Tomasi, M. Cossi, J. M. Millam, M. Klene, C. Adamo, R. Cammi, J. W. Ochterski, R. L. Martin, K. Morokuma, O. Farkas, J. B. Foresman and D. J. Fox, *Gaussian 16 Rev. C.01*, Gaussian Inc., Wallingford, CT, 2016.
48 F. Weigend and R. Ahlrichs, *Phys. Chem. Chem. Phys.*, 2005, **7**, 3297–3305.
49 S. Grimme and M. Waletzke, *J. Chem. Phys.*, 1999, **111**, 5645–5655.
50 I. Lyskov, M. Kleinschmidt and C. M. Marian, *J. Chem. Phys.*, 2016, **144**, 034104.
51 M. Kleinschmidt, J. Tatchen and C. M. Marian, *J. Comput. Chem.*, 2002, **23**, 824–833.
52 M. Kleinschmidt and C. M. Marian, *Chem. Phys.*, 2005, **311**, 71–79.
53 M. Bracker, C. M. Marian and M. Kleinschmidt, *J. Chem. Phys.*, 2021, **155**, 014102.
54 M. Etinski, V. Rai-Constapel and C. M. Marian, *J. Chem. Phys.*, 2014, **140**, 114104.
55 M. Etinski, J. Tatchen and C. M. Marian, *J. Chem. Phys.*, 2011, **134**, 154105.
56 T. Villnow, G. Ryseck, V. Rai-Constapel, C. Marian and P. Gilch, *J. Phys. Chem. A*, 2014, **118**, 11696–11707.
57 B. Bagchi and B. Jana, *Chem. Soc. Rev.*, 2010, **39**, 1936–1954.
58 A. Deshpande, A. Beidoun, A. Penzkofer and G. Wagenblast, *Chem. Phys.*, 1990, **142**, 123–131.
59 O. Peterson, J. Webb, W. McColgin and J. Eberly, *J. Appl. Phys.*, 1971, **42**, 1917–1928.
60 V. Rai-Constapel, S. Salzmann and C. M. Marian, *J. Phys. Chem. A*, 2011, **115**, 8589–8596.
61 A. P. Marchetti and D. R. Kearns, *J. Am. Chem. Soc.*, 1967, **89**, 768–777.
62 Z. Alfassi and C. Previtali, *J. Photochem.*, 1985, **30**, 127–132.
63 S. M. Bachilo and R. B. Weisman, *J. Phys. Chem. A*, 2000, **104**, 7711–7714.
64 N. J. Turro, V. Ramamurthy and J. C. Scaiano, *Principles of Molecular Photochemistry: An Introduction*, University Science Books, 2009.
65 V. Rai-Constapel, T. Villnow, G. Ryseck, P. Gilch and C. M. Marian, *J. Phys. Chem. A*, 2014, **118**, 11708–11717.
66 T. Northey, T. Keane, J. Eng and T. Penfold, *Faraday Discuss.*, 2019, **216**, 395–413.
67 R. Englman and J. Jortner, *Mol. Phys.*, 1970, **18**, 145–164.
68 Z. Murtaza, A. P. Zipp, L. A. Worl, D. Graff, W. E. Jones Jr, W. D. Bates and T. J. Meyer, *J. Am. Chem. Soc.*, 1991, **113**, 5113–5114.
69 T. Zhu and T. Van Voorhis, *J. Phys. Chem. C*, 2019, **123**, 10311–10318.